Electric field and ionization-gradient effects on inertial-confinement-fusion implosions

2009 Plasma Phys. Control. Fusion 51 124048

(http://iopscience.iop.org/0741-3335/51/12/124048)

Plasma Phys. Control. Fusion **51** (2009) 124048 (12pp) doi:10.1088/0741-3335/51/12/124048

Electric field and ionization-gradient effects on inertial-confinement-fusion implosions

P A Amendt[1], J L Milovich[1], S C Wilks[1], C K Li[2], R D Petrasso[2] and F H Séguin[2]

[1] Lawrence Livermore National Laboratory, Livermore CA 94550, USA
[2] Plasma Science and Fusion Center, Massachusetts Institute of Technology, Cambridge MA 02139, USA

E-mail: amendt1@llnl.gov

Received 22 June 2009, in final form 29 July 2009
Published 12 November 2009
Online at stacks.iop.org/PPCF/51/124048

Abstract

The generation of strong, self-generated electric fields (10^8–10^9 V m^{-1}) in direct-drive, inertial-confinement-fusion capsules has been reported (Li *et al* 2008 *Phys. Rev. Lett.* **100** 225001). Various models are considered herein to explain the observed electric field evolution, including the potential roles of electron pressure gradients near the fuel–pusher interface and plasma polarization effects that are predicted to occur across shock fronts (Zel'dovich and Raizer 2002 *Physics of Shock Waves and High-Temperature Hydrodynamic Phenomena* (Mineola, NY: Dover) p 522). In the latter case, strong fields in excess of 10^{10} V m^{-1} and localized to 10–100 nm may be consistent with the data obtained from proton radiography. Such field strengths are similar in magnitude to the criterion for runaway electron generation that could lead to plasma kinetic effects and potential shock-front broadening. The observed electric field generation may also be partly due to plasma ionization gradients localized near the fuel–pusher interface. A model is proposed that allows for differing electron- and ion-density gradient scale lengths in the presence of ionization gradients while preserving overall charge neutrality. Such a redistribution of electrons compared with standard, charge-neutral, single-fluid radiation-hydrodynamics modelling may affect the interpretation of imploded-core x-ray diagnostics as well as alter alpha particle deposition in the thermonuclear fuel.

1. Introduction

The aim of inertial-confinement-fusion (ICF) research is to compress deuterium–tritium (DT) fuel and reach the thermonuclear conditions necessary for ignition, e.g., fuel ion temperatures

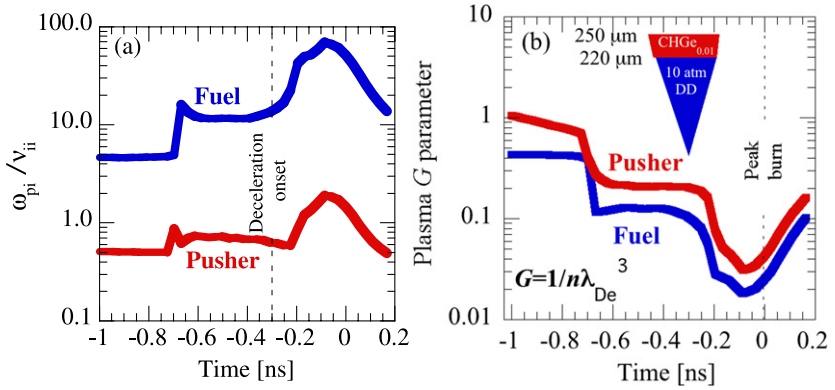

Figure 1. (*a*) Ratio of ion plasma frequency ω_{pi} to ion–ion collision frequency ν_{ii} on fuel- (blue) and pusher- (red) side of interface versus time for plastic capsule [4]. (*b*) Plasma G parameter versus time with capsule diagram inset.

$T_i > 10$ keV and fuel areal densities $\rho R > 0.3$ g cm^{-2} [1]. For cryogenic single-shell capsules the solid fuel shell must be compressed by more than $10^3\times$ in density, corresponding to spherical convergences in excess of ≈30. Much of the fuel compression is from careful (four-) shock sequencing that requires a high-contrast (≈100) laser power history. In the indirect-drive scheme, laser light is incident on a high-Z enclosure or hohlraum for efficient conversion to x rays that quasi-uniformly bathe the centrally placed capsule [1]. In the direct-drive approach, the incident laser energy is absorbed in the capsule shell or ablator [2]. In both approaches, the necessary drive symmetry is arranged by ensuring a sufficient number, optimal placement and adequate power balance of the laser beams. The response of the capsule under these drive conditions is modelled with radiation-hydrodynamics simulations that are based on a set of single-component, charge-neutral fluid equations [3]. Provided the collisionality of the underlying plasma is sufficiently high, such an Euler-based description is often adequate. For describing instability growth the representative timescale is an inverse ion plasma frequency ω_{pi}^{-1} due to the importance of ion inertia. When the ion–ion collision frequency of the plasma is large compared with ω_{pi}, the fluid approximation suffices and plasma effects are deemed negligible. However, there are examples where such an approximation is not well obeyed. Consider the behaviour of an ICF, Omega-scale, indirect-drive, plastic capsule [1, 4] as shown in figure 1. The ratio of the ion plasma frequency to the ion-collision frequency is plotted versus time relative to the instant of peak neutron production. For several hundred picoseconds before and following deceleration onset, the deuterium fuel is collisionless while the pusher is only marginally collisional. This interval near and after deceleration onset is of key concern for stability considerations because Rayleigh–Taylor growth typically begins to dominate over this time [5]. Figure 1(*b*) shows the so-called plasma G parameter that is a measure of the (reciprocal) number of electrons contained within a Debye 'cube'. The criterion for classical plasma behaviour is that $G \ll 1$, ensuring that collective behaviour dominates over binary collisional effects. Equivalently, such a criterion lends statistical meaning to a Debye length ($\lambda_{De} = \sqrt{k_B T_e/4\pi n_e e^2}$, where n_e is the electron density and T_e the electron temperature) as a valid metric for gauging the screening of plasma electric fields. Inspection of figure 1(*b*) shows that both the fuel and the pusher satisfy this classical plasma criterion. In sum, the capsule in non-cryogenic ICF experiments can behave as a quasi-collisionless, classical plasma.

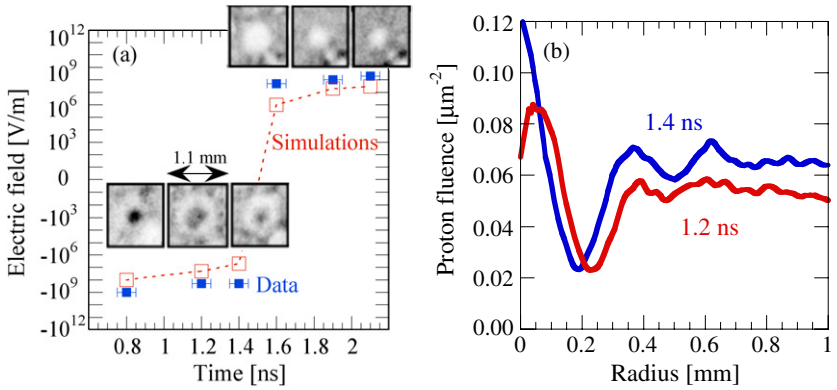

Figure 2. (*a*) Inferred (blue) and simulated (red) electric field versus time with overlaid proton fluence images [6]. (*b*) Angle-averaged proton signal lineouts from [6] at 1.2 ns (red) and 1.4 ns (blue).

Backlighting an imploding capsule with 15 MeV protons provides the first direct evidence of significantly large electric fields in ICF targets [6]. The presence of such fields, irrespective of their exact origin and degree of localization, implies a departure from perfect charge neutrality as implicitly assumed in mainline radiation-hydrodynamics simulations [3]. The consequences of these large electric fields on various aspects of ICF capsule performance have not yet been thoroughly explored. The aim of this paper is to provide clues to answering two particular questions. First, an assessment of the effects of such fields on capsule performance will rely on their nature and origin. If the fields are localized to a shock front, what could be their consequences, if any, on shock propagation, uniformity and front broadening? Second, the presence of electric fields will necessarily give rise to local charge imbalances. What is their effect on redistributing electrons while preserving global charge neutrality? The answer could affect our interpretation of implosion dynamics based on x-ray imaging methods such as Compton radiography. Section 2 considers various scenarios for electric field generation as constrained by the recent proton radiographic data [6]. The conclusion is that electric field generation induced by electron pressure gradients alone is not sufficient to explain the inferred values of the field, leaving a potentially strong role for shock-front field generation. Section 3 explores the consequences of a local charge imbalance on modified electron and ion distributions. When a gradient in the average ionization state of the ions occurs, significant differences between the electron- and ion-density gradient scale lengths become possible. A new plasma parameter is derived which dictates the size of the mismatch: $\varepsilon \equiv \zeta L_{n_e}^2/\lambda_{De}^2$, where $\zeta \ll 1$ is the normalized charge imbalance and $L_{n_e} \gg \lambda_{De}$ is the electron gradient scale length. We summarize our conclusions in section 4.

2. Electric field generation

Figure 2 reproduces the history of the inferred electric field for a direct-drive plastic (CH) capsule [6] (where a minus sign denotes a field pointing *towards* the origin). The electric field was ascribed to acceleration-induced electron pressure gradients in this analysis [6]. Here, we analytically develop and extend this argument, as well as consider other candidate field-generating mechanisms.

2.1. ∇P_e*-field generation*

In a co-moving (shell) reference frame, momentum balance for the ions and electrons together yields

$$0 = \frac{-\nabla P}{\rho} - \vec{g}, \tag{1}$$

where P is the total kinetic pressure (electron and ion), ρ is the ion mass density, $\vec{g}$ is the radial acceleration near the fuel–pusher interface and the electrons are assumed massless (but see section 3). Using that the electron pressure $P_{ej} = P \cdot Z_j/(1+Z_j)$, where Z_j is the average ionization state of the ions in region j, assuming nearly equal ion and electron temperatures ($T_{ij} \cong T_{ej}$), and combining electron momentum balance (or the Boltzmann relation: $\vec{E}_j = -\nabla P_{ej}/en_{ej}$) with equation (1), we find

$$E_j = \frac{gM_j}{e\left(1+Z_j\right)} - \frac{P_{ej}}{Z_j e n_{ej}} \cdot \frac{\nabla Z_j}{1+Z_j}. \tag{2}$$

Here, E_j is the radial electric field on the jth side of the interface, n_{ej} is the electron number density, $-e$ is the electron charge, M_j is the average mass of the ions in region j, and ideal equations of state are assumed. The first term on the right-hand side of equation (2) is an acceleration-driven source for the self-generated electric field as proposed earlier [6], whereas the last term is due to ionization gradients. In typical indirect-drive (as well as direct-drive [7]) ICF experiments with CH shells and H_2 fuel fill, $g \approx 1 \times 10^{17}\,\mathrm{cm\,s^{-2}}$, $\langle Z_2 \rangle \cong 3.5$ and $M_2 = 6.5$ in proton mass units, giving in the pusher ($j = 2$) after deceleration onset, $E_2 \approx 1.6 \times 10^7\,\mathrm{V\,m^{-1}}$ from the acceleration-driven source term alone. This contribution to the electric field falls short of the inferred peak values [6] by almost two orders of magnitude. However, a large gradient in ionization occurs on the interface between the fuel and the pusher from the step-like difference in average ionization states, leading to an effective discontinuity in the electron and ion partial pressures:

$$\Delta P_e \equiv P_{e2} - P_{e1} = \frac{P_{e1} \cdot (Z_2 - Z_1)}{Z_1 \cdot (1+Z_2)} = -\Delta P_i. \tag{3}$$

Across the fuel–pusher interface, ambipolar diffusion will give rise to an interpenetration distance

$$\Delta_j(\mu\mathrm{m}) \approx 2\tau^{1/2}(\mathrm{ns}) \cdot \left(\frac{T_{ej}(\mathrm{heV})}{A_j^{1/4} Z_j^2 n_{ij}^{1/2} \left(10^{22}\,\mathrm{cm^{-3}}\right) \cdot \sqrt{\ln \Lambda_j}} \right) \tag{4}$$

in a time τ after shock breakout but before deceleration onset ($\vec{g} = 0$) [8]. Here $\Lambda_j = (3/2)\sqrt{k_B^3 T_{ej}^3/\pi n_{ej}}/Z_j e^3$ is the Coulomb logarithm ≈3–5 [8], A_j is the average atomic weight in region j, the electron temperature is in units of hecto-electron volts, i.e., 1 heV = 100 eV and $T_{ej} \cong T_{ij}$ is taken. Under typical capsule conditions ($T_{e1} \approx T_{e2} \cong 0.6$ heV, $n_{e1} \cong 2 \times 10^{22}\,\mathrm{cm^{-3}}$, $n_{e2} \cong 3 \times 10^{22}\,\mathrm{cm^{-3}}$) before deceleration onset, the ionization boundary is expected to broaden by as much as a micrometre on the fuel side ($j = 1$), but only ≈0.03 μm on the pusher side. Using $P_{ij} \approx \rho_j C_{sj}^2 (T_{ij}/T_{ej})/Z_j$, where C_{sj} is the isothermal ion sound speed, we rewrite equation (2) for the electric field by using equation (4):

$$E_j(\mathrm{V\,m^{-1}}) = 1.04 \times 10^7 \left\{ \frac{A_j g \left(10^{17}\,\mathrm{cm\,s^{-2}}\right)}{1+Z_j} \right\} - 2.5 \times 10^8 \left\{ \frac{A_j^{1/4} Z_j n_{ij}^{1/2} (10^{23}\,\mathrm{cm^{-3}})}{\sqrt{\tau\,(\mathrm{ns})}} \right\} \cdot \frac{\delta Z_j}{1+Z_j} \cdot \sqrt{\ln \Lambda_j}, \tag{5}$$

where $\delta Z_j \cong 2.5$ is the stepwise change in Z_j across the fuel–pusher boundary layer, and the 'interface' is identified with the location of the mean value of Z_j, i.e. $\sum Z_j/2$. We immediately see that the second term on the right-hand side dominates and has the same sign as the first term during the early acceleration stage ($g < 0$). The reported electric field values $\approx -10^9\,\mathrm{V\,m^{-1}}$ [6] (cf figure 2(*a*)) are essentially obtained from the expression $2E \cdot L_{\mathrm{chord}} = \varepsilon_{\mathrm{p}} \tan\theta/e$ for the transverse potential change in a transiting proton, where ε_{p} is the imaging proton energy ($\approx$15 MeV), L_{chord} is the proton chord length through (half) the electric field region and θ is the deflection angle of the protons exiting the capsule [6]. If Δ is the total width of the (annular) field-generating region, then the maximum chord length for a deflected proton is $\max(L_{\mathrm{chord}}) = \sqrt{2R \cdot \Delta + \Delta^2}$, where R is the fuel radius. When $\max(L_{\mathrm{chord}})$ is chosen as a fuel radius ($\approx$100–200 μm) as in [6], the inferred field strengths are arguably a lower bound. The field strength depends on the size of Δ for each candidate source of field generation considered. For instance, the scale length Δ associated with the first term on the right-hand side of equation (5) varies as $\approx C_{sj}^2/g$ which is on the order of 10 μm or more; for the second term, the scale length on the pusher (fuel) side is $\approx$0.03 (0.5) μm, cf equation (4). For this latter case, the chord length is $\approx$3 (10) μm, leading to fields greater than $10^8\,\mathrm{V\,m^{-1}}$ on the pusher side and more than 10$\times$ larger than the (acceleration-driven) first term. This value for the electric field is considerably less than the theoretical limit on the maximum self-generated electric field as follows. Potential changes $\Delta\Phi$ on the order of $k_{\mathrm{B}}T_{\mathrm{e}}/e$ are expected to leak into the plasma because of incomplete charge screening from the thermal electrons, with a minimum spatial scale on the order of a Debye length. For $T_{\mathrm{e}} \approx 1$ heV, $n_{\mathrm{e}} \approx 10^{23}\,\mathrm{cm^{-3}}$, the resulting maximum electric field is $\approx 4 \times 10^{11}\,\mathrm{V\,m^{-1}}$.

A strong ionization gradient at the fuel–pusher interface yields a negative sign for the electric field in accord with the data up to deceleration onset (see figure 2(*a*)). However, this effect cannot explain the abrupt sign change observed near deceleration onset. Mix from Rayleigh–Taylor instability after deceleration onset will further blur this interface over 5–10 μm, thereby significantly reducing the strength of the ionization-gradient generation mechanism; moreover, the sign of the gradient of Z is unchanged at this interface. The conclusion is that electric field generation by ∇P_{e} is either too small to wholly explain the data (via the acceleration-driven term) or is unable to accommodate the observed sign change (from ionization gradients alone).

2.2. *Non-∇P_{e} field generation*

Another candidate mechanism for electric field generation, independent of the electron pressure gradient, is from an acceleration-induced charge separation at the fuel–pusher interface. The electrons in the pusher will advance slightly ahead of the ions due to their comparatively low mass, only to have their motion quickly arrested by collisions or self-electric fields. Note that this spatial separation follows the sign of the shell acceleration. The electrons reach a terminal speed $v_{\mathrm{term}} = g \cdot (M_j/m_{\mathrm{e}})\tau_{\mathrm{es}}$ well within the time scale for ions to inertially respond $1/\omega_{\mathrm{pi}\,j}$, where τ_{es} is an electron (slowing-down) time scale [8] and $\omega_{\mathrm{pi}\,j} = \sqrt{4\pi n_{\mathrm{e}\,j} Z_j e^2/M_j}$ is the ion plasma frequency in region j. Thus, the charge-separation distance Δx is expected to scale as $v_{\mathrm{term}}/\omega_{\mathrm{pi}\,j} \leqslant \lambda_{\mathrm{De}}$ which is on the order of 10^{-8} cm. Using Gauss's law ($E \cong -4\pi e(n_{\mathrm{e}2} - n_{\mathrm{e}1})\Delta x$) we find an electric field on the order of $10^9\,\mathrm{V\,m^{-1}}$. The change in potential due to field deflection $\Delta\Phi_{\mathrm{t}} \equiv 2E \cdot \max(L_{\mathrm{chord}})$ is $\approx 2 \times 10^3$ V which is still less than the $\cong 10^4$–10^5 V that were measured [6].

We can estimate the representative scale length of field generation by using that self-generated potential perturbations in the plasma significantly greater than order $k_{\mathrm{B}}T_{\mathrm{e}}/e$ are

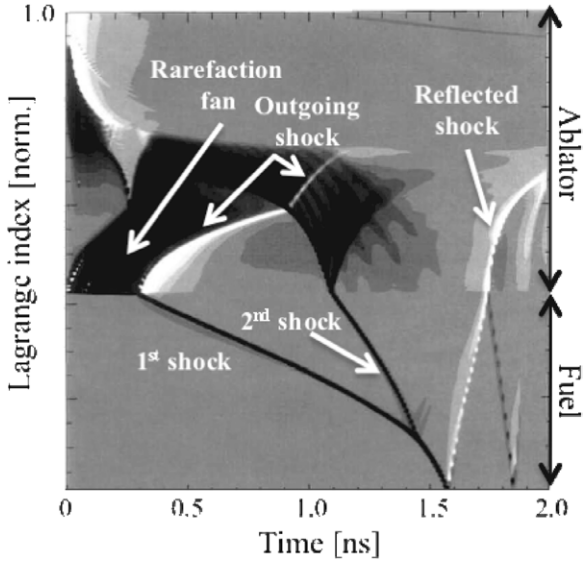

Figure 3. Simulated streak plot of logarithmic derivative of the pressure showing shocks and rarefactions for direct-drive target of [6].

energetically unfavourable. Thus, we can write $k_B T_e/e \approx E \cdot \Delta = \Delta\Phi_t \cdot \Delta/[2\max(L_{chord})] \cong \Delta\Phi_t\sqrt{\Delta/8R}$, whence $\Delta/R = 8T_e^2(\text{eV})/\Delta\Phi_t^2(\text{V})$. With T_e in the range 20–100 eV for times of interest in the implosion and $\Delta\Phi_t \cong 10^4$–10^5 V from experiment [6], we obtain $\Delta \ll 1\,\mu$m for $R = 200\,\mu$m. Such an inferred range of scale lengths for field generation is consistent with a Debye screening or shock-front origin.

2.3. Shock-driven field generation

A third candidate mechanism for field generation is from plasma polarization within a shock front [9]. The electrons, being more mobile than the ions, will diffuse ahead of the shocked ions in response to the characteristically strong density gradients and, in turn, establish an electric field. The departure from charge neutrality ($\delta n_e/n_e$) over a diffusion length scales as $\lambda_{De}^2/\ell_{mfp}^2$, where ℓ_{mfp} is the ion–ion collisional mean free path. The potential difference across the shock $\Delta\Phi_{21}$ is determined from the work done per electron in compressing the upstream ('1') electron gas: $\Delta\Phi_{21} \approx (k_B T_e/e) \cdot \ln(\rho_2/\rho_1) \cong k_B T_e/e$, where T_e is the post-shock ('2') electron temperature. The associated electric field strength is

$$|\vec{E}| \approx \Delta\Phi_{21}/\ell_{mfp} \approx \frac{n_e Z^3 e^3 \ln\Lambda}{k_B T_e}$$
$$= 2.07 \times 10^{10} \cdot Z^3 \cdot \left(\frac{n_e(10^{22}\,\text{cm}^{-3})\ln\Lambda}{T_e(\text{eV})}\right)(\text{V m}^{-1}). \quad (6)$$

The electric field points in the direction of shock propagation, reversing sign as the first shock in the capsule fuel reflects off the origin. As shown in figure 3, the predicted time difference between shock convergence (at the origin) and deceleration onset (when the outgoing shock reaches the fuel–pusher interface) is less than 200 ps. Consequently, the observed abrupt sign change in $\vec{E}$ may be compatible with shock reversal in the fuel. A further noteworthy feature is found in figure 2(*a*) at 1.2 ns where a bright annulus of proton (fluence) deficit is

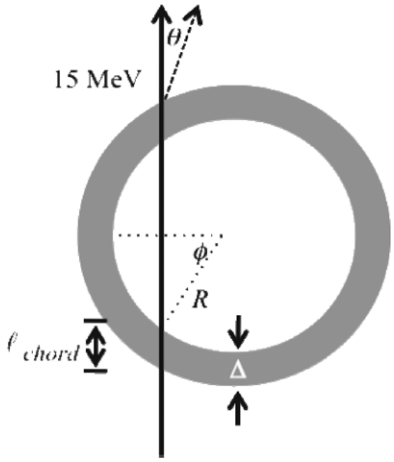

Figure 4. Schematic of geometry used to evaluate chord length versus incidence angle ϕ.

perceptible outside the central, dark area of elevated proton fluence. Referring back to figure 3, an outgoing shock is seen in the capsule shell near this time, suggesting a possible contribution to this annular feature beyond the local deficit of protons produced by an interior focusing field.

The magnitude of the self-generated electric field predicted by equation (6) is typically on the order of 10^{10} V in the fuel, and possibly as high as 10^{11} V in the CH pusher ($Z \approx 3.5$). The ion–ion mean free path $\ell_{\rm mfp} \cong 10$ nm corresponds to a maximum chord length of nearly 2 μm in the fuel for a fuel radius of $\approx$200 μm. Interestingly, the predicted transverse potential $\Delta\Phi_{\rm t} = 2E \cdot \max(\ell_{\rm chord})$ for the deflected protons is close to the measured 10^5 V [6]. It is of interest to evaluate the runaway electric field E_r that occurs when the electrons are able to accelerate by a thermal speed or more over an electron collision time: $E_r \approx 0.2Ze \ln\Lambda/\lambda_{\rm De}^2$ [8]. Comparison with equation (6) shows that the shock-front generated electric field is a fixed fraction of E_r at 40% for $Z = 1$ (fuel) and larger for $Z > 1$ (shell). Consequently, a large fraction of the electrons in the shock front are capable of becoming a 'hot' runaway population that could self-consistently alter the shock profile through a resulting redistribution of the ions. Particle-in-cell simulations are in progress with large-scale plasma (LSP) simulations [10][3] to assess the role of charge polarization and kinetic effects on the evolution of a plasma shock front.

2.4. Simulated proton deflectometry

We have considered three scenarios for electric field generation: a $\nabla P_{\rm e}$-driven mechanism, interfacial charge separation and shock-front polarization. To help distinguish between these three candidate sources, a simple model simulating the proton fluence at the detector plane behind the subject target (30.9 cm) is used. Figure 4 shows the geometry used in our model with the chord length given analytically as

$$\frac{\ell_{\rm chord}}{R} = \sqrt{\left(\frac{\Delta}{R}\right)^2 + 2\left(\frac{\Delta}{R}\right)(1-\sin\phi)}. \tag{7}$$

[3] LSP is a software product of ATK Mission Research.

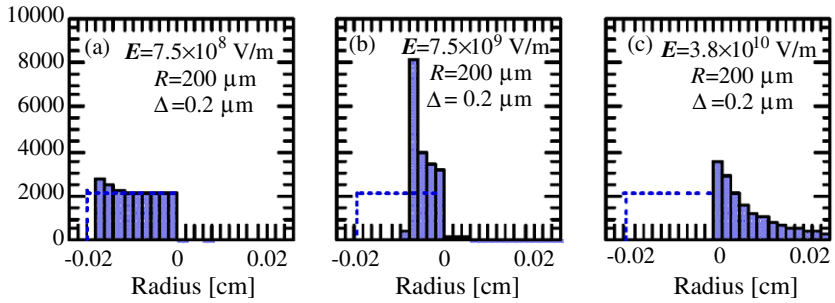

Figure 5. Histograms of deflected protons at detector plane for annular thickness of Δ=0.2 μm, annular radius of $R = 200\,\mu$m and three values of radial electric field $\boldsymbol{E}$. Dashed line denotes incident proton distribution.

The underlying assumptions are that the electric field is uniform over an annulus of thickness Δ and the change in proton trajectory *within* the annulus as a function of distance along the chord length can be neglected to a good approximation. Three-dimensional effects from geometric (spherical) convergence near the origin and backlighter divergence at the target plane are ignored in this treatment. A set of 15 MeV backlighter protons is uniformly incident on the (left-half side of the) shell, and the deflected protons are binned over 20 μm steps to simulate a distribution at the detector position. Figure 5 shows three examples for $\Delta/R = 0.001$ and $R = 200\,\mu$m, corresponding to $\approx$1.2–1.4 ns in the data [6], versus increasing electric field strength. An electric field of less than 10^9 V m^{-1} shows very little deflection, while a 10$\times$ increase shows a significant narrowing of the distribution and signal contrast that is qualitatively consistent with the data (see figure 2(*b*)) and in good agreement with the measured transverse potential change $E \cdot \max(2L_{\rm chord})$ of $\approx 10^5$ V [6]. A further five-fold increase in the electric field predicts excessive deflection, leading to a degree of (high) spatial broadening and (low) signal contrast not seen experimentally, cf figure 2(*b*). Figures 6(*a*)–(*c*) show the dependence of the proton distribution versus annular width at fixed $E \cdot \Delta$. A very mild trend of *increasing* signal contrast with decreasing annular width is suggested. Although this comparison does not establish or distinguish a particular field generation mechanism, the indication is that the field strengths in the capsule are consistent with $\approx 10^{10}$ V m^{-1} near 1.2–1.4 ns, which is consistent with the shock-front field generation scenario (section 2.3). The effective annular width of the field-generating region is still undetermined, but the results from this exercise are arguably more consistent with shock-front field generation. Figure 7 shows the combined effects of spatial blurring from finite source size, proton scattering and instrumental broadening of the signal as described in [6] when applied to the simulated data shown in figure 5. We find that too small or too large an electric field gives minimal levels of signal contrast, while the intermediate case (figure 5(*b*)) gives a synthetic profile in fairly good agreement with the data as depicted in figure 2(*b*). Parenthetically, the transverse potential change $E \cdot \max(2L_{\rm chord})$ was measured to be $\approx 10^5$ V [6], which agrees with the intermediate strength case (cf figures 5(*b*) and 7(*b*)).

3. Plasma profile modification from nonzero ∇Z

Accelerating plasmas as in an ICF capsule can generate intrinsic charge separations. From Gauss's law $\nabla \cdot \vec{E} = 4\pi e n_{\rm e}(Z n_{\rm i}/n_{\rm e} - 1) \equiv 4\pi e n_{\rm e}\zeta$, we can roughly estimate for the charge

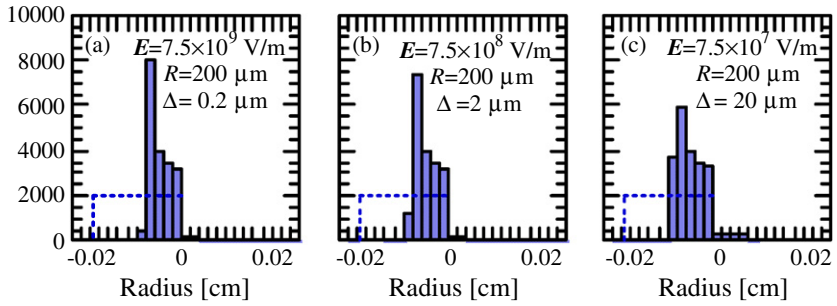

Figure 6. Histograms of proton counts at detector for fixed product of field strength $\boldsymbol{E}$ and annular width Δ.

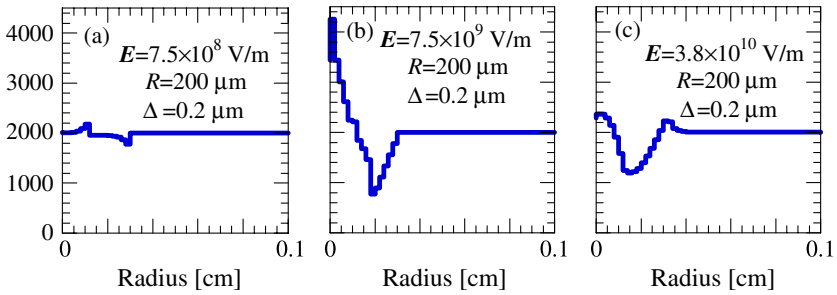

Figure 7. Spatial blurring applied to figure 5 with half-width half-maximum smearing length of $\approx 100\,\mu$m.

Table 1. Typical parameters for capsule and hohlraum wall plasmas.

	g (cm s^{-2})	λ_{De} (nm)	C_s (cm s^{-1})	ζ
Capsule	10^{17}	0.7	1×10^7	10^{-9}
Hohlraum	10^{16}	300	2×10^7	10^{-6}

imbalance parameter ζ by using the electron Boltzmann relation:

$$|\zeta| \approx \frac{|E|}{4\pi e n_e L_{n_e}} \approx \frac{|\nabla P_e|}{4\pi e^2 n_e^2 L_{n_e}} \approx \frac{\lambda_{De}^2}{L_{n_e}^2}, \tag{8}$$

where L_{n_e} is the electron density-gradient scale length and T_e is taken as nearly constant. From the above definition of ζ we can write the (inverse) ionization-gradient scale length

$$\frac{1}{L_Z} = \frac{1}{L_{n_e}} - \frac{1}{L_{n_i}} + \left(\frac{\zeta}{1+\zeta}\right) \cdot \frac{1}{L_\zeta} \tag{9}$$

in terms of the remaining inverse-gradient scale lengths $L_{n_e}^{-1}$, $L_{n_i}^{-1}$, L_ζ^{-1}. For $\zeta \ll 1$ and with $L_\zeta \geqslant \lambda_{De}$, the last term on the right-hand side of equation (9) can be neglected. Furthermore, if $L_{n_e}, L_{n_i} \ll L_Z$, then $L_{n_e} \approx L_{n_i} \cong C_s^2/g$ from equation (1) for $ZT_e > T_i$, and equation (8) leads to a new plasma parameter

$$\zeta = \frac{\lambda_{De}^2 g^2}{C_s^4}. \tag{10}$$

Table 1 shows expected values of λ_{De}, g, C_s and ζ for an ICF capsule fuel and hohlraum wall blowoff plasma. We mention that the acceleration-driven charge imbalance level captured by

equation (10) is in addition to statistical fluctuations that occur in any local thermodynamic equilibrium (LTE) plasma. The effects of a small, but finite, charge imbalance level ζ on plasma motion can be readily assessed. Euler's equation for the average hydrodynamic motion, including charge imbalance, takes the form (cf equation (1)):

$$\frac{\mathrm{d}\vec{v}}{\mathrm{d}t} = -\frac{\nabla P}{\rho} + \zeta \cdot \frac{Ze\vec{E}}{M}, \tag{11}$$

where the ion equation of motion $\frac{\mathrm{d}\vec{v}_\mathrm{i}}{\mathrm{d}t} = -\frac{\nabla P_\mathrm{i}}{\rho} + \frac{Ze\vec{E}}{M}$ has been combined with the (electron) Boltzmann relation, $\vec{v} \equiv \vec{v}_\mathrm{i} + (Zm_\mathrm{e}/M) \cdot \vec{v}_\mathrm{e}$, and $\vec{v}_\mathrm{e}$ is the electron fluid speed. For field strengths $\cong 10^{10}\,\mathrm{V\,m^{-1}}$ and accelerations $\cong 10^{17}\,\mathrm{cm\,s^{-2}}$, the last term in equation (11) becomes important only when ζ approaches or exceeds $\cong 10^{-4}$. Curiously, an identification of the average fluid speed $\vec{v}$ with $\vec{v}_\mathrm{i}$ in an Euler-based fluid description is valid provided $\left|\vec{v}_\mathrm{e}\right| \ll (M/m_\mathrm{e}Z) \cdot \left|\vec{v}_\mathrm{i}\right|$. In a statistically averaged, root-mean-squared (LTE) sense, this condition is met when $Z\sqrt{(m_\mathrm{e}/M) \cdot (T_\mathrm{e}/T_\mathrm{i})} \ll 1$. However, there are physical circumstances when this condition may not be well satisfied—such as in the low-density, high-Z, hohlraum blowoff plasma where often $T_\mathrm{e} \gg T_\mathrm{i}$, according to radiation-hydrodynamics simulations. Moreover, plasma kinetic phenomena may arise in which a significant population of hot electrons violates the LTE approximation and the condition: $|\vec{v}_\mathrm{e}| \ll (M/m_\mathrm{e}Z) \cdot |\vec{v}_\mathrm{i}|$. Despite these caveats, we presume that the *average* flow in a single-fluid description or Euler sense is unaffected by fields, but a redistribution of the charged species is allowed—particularly when a variation in the ionization state ($\nabla Z \neq 0$) exists—as we now show.

From the electron Boltzmann relation and Gauss' law we obtain

$$\zeta = \frac{\nabla \cdot \vec{E}}{4\pi e n_\mathrm{e}} = \frac{\vec{g} \cdot \nabla Z}{\omega_\mathrm{pi}^2} \frac{(1-Z)}{(1+Z)^2} + \frac{\lambda_\mathrm{De}^2}{Z\,(1+Z)} \cdot \left(\frac{\nabla Z \cdot \nabla n_\mathrm{e}}{n_\mathrm{e}} + \frac{2\,|\nabla Z|^2}{(1+Z)} - \nabla^2 Z \right). \tag{12}$$

Note that nonzero ∇Z is closely identified with finite ζ or charge separation, and no assumption on the electron temperature profile has been made here. Upon approximating the various gradient terms with average scale lengths, making use of equation (9) with $\zeta \ll 1$, and rearranging terms, we find

$$1 - \frac{L_{n_\mathrm{e}}}{L_{n_\mathrm{i}}} = \zeta \cdot \left(\frac{L_{n_\mathrm{e}}}{\lambda_\mathrm{De}} \right)^2 \cdot \frac{2\,(1+Z)}{\left[1 + B + \sqrt{(1+B)^2 - 4\zeta\,Z\,(1-Z)\,L_{n_\mathrm{e}}^2/\lambda_\mathrm{De}^2} \right]}, \tag{13}$$

where $B \equiv \frac{L_{n_\mathrm{e}} g}{C_s^2} \cdot \frac{Z(1-Z)}{1+Z}$. Equation (13) shows that the electron- and ion-density profiles can differ (when $L_Z < \infty$) by an amount proportional to $\varepsilon \equiv \zeta L_{n_\mathrm{e}}^2/\lambda_\mathrm{De}^2$. For capsule (hohlraum wall) plasmas, ε is in the range 0.1–1 for $L_{n_\mathrm{e}} \cong 10\ (100)\,\mu\mathrm{m}$, according to table 1. Note that such a scale-length mismatch does *not* lead to unphysical, large charge imbalances in the linear approximation:

$$\begin{aligned} \zeta(x) &\cong \frac{Z_0 n_{\mathrm{i}0}}{n_{\mathrm{e}0}} \cdot \left(1 + \frac{x}{L_Z} + \cdots \right) \left(1 + \frac{x}{L_{n_\mathrm{i}}} + \cdots \right) \left(1 - \frac{x}{L_{n_\mathrm{e}}} + \cdots \right) - 1 \\ &= \zeta_0 + O(x^2), \end{aligned} \tag{14}$$

where equation (9) has been used. We evaluate equation (13) in two limits:

$$\frac{4\varepsilon Z(Z-1)}{(1+B)^2} \gg 1 : 1 - \frac{L_{n_e}}{L_{n_i}} = \sqrt{\varepsilon \cdot \left[\frac{1+Z}{Z(Z-1)}\right]}; \tag{15a}$$

$$\frac{4\varepsilon Z(1-Z)}{(1+B)^2} \ll 1 : \quad 1 - \frac{L_{n_e}}{L_{n_i}} = \varepsilon \cdot \left(\frac{1+Z}{1+B}\right). \tag{15b}$$

The second limiting case (equation (15*b*)) is more typical of ICF capsule and hohlraum conditions. For fully ionized DT fuel or a hydrogen gas fill in a hohlraum ($T_e \gg 13\,\mathrm{eV}$), ionization gradients are non-existent, and the electron and ion profiles are almost exactly charge compensating. For lower temperature thermonuclear fuels, the capsule shell and the ablated hohlraum wall, a significant mismatch between the electron and ion profiles is possible. For example, such a potential redistribution of the electrons could affect the interpretation of diagnostic signatures based on electron self-emission that are used to infer aspects of implosion dynamics [11]. Alpha particle stopping depends mostly on electron scattering below $T_e = 20\,\mathrm{keV}$, so any regions of incomplete ionization could lead to a redistributed electron population and possibly altered burn propagation.

4. Summary

A wealth of recent data on electric fields in capsules [6] and hohlraums [12] motivates further study to assess their potential impact on implosion dynamics. The reported $\approx 10^5\,\mathrm{eV}$ peak transverse energy E_{trans} of deflected 15 MeV protons means that fuel ions can acquire radially directed energy in the field-generating region of dimension Δ by the amount: $E_{\mathrm{trans}}\sqrt{\Delta/8R}$. Knowledge of the field-generating mechanism and its spatial extent is needed to estimate the energy gain of such ions and their potential impact as a source of fuel preheat. A simple argument based on the maximum expected levels of self-generated potential ($\approx k_B T_e/e$) in a plasma shows that sub-micrometre scale lengths for field generation are consistent with the measured value of E_{trans}.

A variety of field-generating scenarios are considered, including a ∇P_e-based mechanism, interfacial charge separation from shell acceleration and shock-front polarization. Field generation from the acceleration component ($\propto \vec{g}$) of ∇P_e can account for the observed change in sign near deceleration onset but is typically too weak by one-to-two orders of magnitude. The ionization component ($\propto \nabla Z$) of ∇P_e yields larger field strengths but fails to reproduce the sign change. An acceleration-induced charge separation at the fuel–pusher interface is shown to produce $\approx 10^9\,\mathrm{V\,m^{-1}}$ fields, but localized only over $10^{-8}\,\mathrm{cm}$. Larger fields with greater spatial extent are predicted for polarized shock fronts. In the latter case the predicted field strengths are competitive with the threshold values for generating runaway electrons, potentially giving rise to kinetic phenomena that may manifest as shock-front broadening.

A simple proton deflectometry analysis is undertaken to help elucidate the underlying field generation mechanism. Comparison of the predicted proton fluence distribution with the data suggests that field strengths $\approx 10^{10}\,\mathrm{V\,m^{-1}}$ over a 200 nm extent are plausible and arguably more consistent with the shock-front generation scenario. A favourable, though weak, trend of increasing signal contrast with decreasing annulus width is also shown.

For electron pressure-gradient driven electric fields a relation between ionization gradients and local charge imbalance is obtained. Further analysis establishes a key plasma parameter $\varepsilon = \zeta \cdot (L_{n_e}/\lambda_{De})^2$ governing the mismatch between electron- and ion-density profiles that can be significant in ICF capsule and hohlraum plasmas. An important plasma effect occurs when $T_e/T_i \gg 1$ and $Z \gg 1$, potentially leading to a significant difference between the

ion fluid velocity $\vec{v}_{\rm i}$ and the Euler fluid velocity $\vec{v} = \vec{v}_{\rm i} + (Zm_{\rm e}/M) \cdot \vec{v}_{\rm e}$, despite the large ion-to-electron mass ratio. Such a difference is not presently considered in state-of-the-art radiation-hydrodynamic simulations [3].

Acknowledgments

Useful discussions with Nino Landen are gratefully acknowledged. This work performed under the auspices of the Lawrence Livermore National Security, LLC (LLNS) under Contract DE-AC52-07NA27344 and supported by LDRD-08-ERD-062.

References

[1] Lindl J D *et al* 2004 *Phys. Plasmas* **11** 339
[2] Soures J M *et al* 1996 *Phys. Plasmas* **3** 2108
[3] Marinak M M *et al* 2001 *Phys. Plasmas* **8** 2275
[4] Amendt P A *et al* 2002 *Phys. Rev. Lett.* **89** 165001
[5] Amendt P A 2008 *Phys. Rev. Lett.* **101** 115004
[6] Rygg J R *et al* 2008 *Science* **319** 1223
Li C K 2008 *Phys. Rev. Lett.* **100** 225001
[7] Radha P B *et al* 2005 *Phys. Plasmas* **12** 032702
[8] Krall N A and Trivelpiece A W 1973 *Principles of Plasma Physics* (New York: McGraw-Hill)
[9] Zel'dovich Ya B and Raizer Yu P 2002 *Physics of Shock Waves and High-Temperature Hydrodynamic Phenomena* (Mineola, NY: Dover) p 522
See also Jaffrin M Y and Probstein R F 1964 *Phys. Fluids* **7** 1658
Yemin H and Xiwei H 2003 *Phys. Plasmas* **10** 2704
He Y, Hu X, Jiang Z and Lü J 2008 *Phys. Plasmas* **15** 012111
[10] Welch D R *et al* 2001 *Nucl. Instrum. Methods Phys. Res.* A **464** 134
[11] Koch J A *et al* 2008 *High Energy Density Phys.* **4** 1
[12] Li C K *et al* 2009 *Phys. Rev. Lett.* **102** 205001